Droplets and Bubbles in Microfluidic Devices

Shelley Lynn Anna

Center for Complex Fluids Engineering, Carnegie Mellon University, Pittsburgh, Pennsylvania 15213; email: sanna@cmu.edu

Annu. Rev. Fluid Mech. 2016. 48:285–309

First published online as a Review in Advance on September 21, 2015

The *Annual Review of Fluid Mechanics* is online at fluid.annualreviews.org

This article's doi: 10.1146/annurev-fluid-122414-034425

Keywords

emulsion, foam, interfacial tension, surfactant, hydraulic network

Abstract

Precise, tunable emulsions and foams produced in microfluidic geometries have found wide application in biochemical analysis and materials synthesis and characterization. Superb control of the volume, uniformity, and generation rate of droplets and bubbles arises from unique features of the microscale behavior of fluid interfaces. Fluid interfaces confined within microfluidic channels behave quite differently than their counterparts in unbounded flows. Confinement inhibits capillary instabilities so that breakup occurs by largely quasi-static mechanisms. The three-dimensional flow near confined interfaces in rectangular geometries and feedback effects from resistance changes in the entire microfluidic network play important roles in regulating the interfacial deformation. Timescales for transport of surfactants and particles to interfaces compete with flow timescales at the microscale, providing further opportunity for tuning the interfacial coverage and properties of individual droplets and bubbles.

1. INTRODUCTION

Droplets and bubbles can be generated in microfluidic devices with unprecedented uniformity and control over the volume and frequency of production. Early work showed the potential and excitement of droplets at the microscale (Anna et al. 2003, Sugiura et al. 2001, Thorsen et al. 2001), and the ease of soft lithography fabrication methods (McDonald et al. 2000, Whitesides & Stroock 2001) and high-speed visualization has spurred rapid advancements in both applications and our fundamental understanding of multiphase phenomena. Droplets have been used as discrete chemical and biological reactors for protein crystallization, nanoparticle synthesis, enzyme kinetics studies, and cell culture, among others (Koester et al. 2008, Song et al. 2006). The high degree of monodispersity inherent in microfluidic production allows droplets and bubbles to self-assemble into one-dimensional (1D), 2D, and 3D crystal-like structures that are useful in the rapid analysis of many simultaneous reactions (Pompano et al. 2011). Performance metrics for droplet-based assays have been quantified, and strategies for optimizing their design have been identified (Rosenfeld et al. 2014). The effective design of multiphase microfluidic devices hinges in part on a deeper understanding of the mechanisms driving the formation and motion of droplets and bubbles at these length scales. Accurate scaling analyses and models incorporating all of the relevant phenomena that influence the droplet volume, production rate, and monodispersity provide important criteria for the design and optimization of droplet-based assays and devices.

The present review focuses on the fluid dynamical and interfacial phenomena underlying the use of planar microfluidic devices to generate droplets and bubbles in a continuous phase of immiscible liquid. It considers only situations in which the droplets and bubbles are fully encapsulated by the surrounding liquid and no contact lines are present; gravity and inertia are small or negligible; and phenomena occur passively, without external input or external fields. In these situations, droplet and bubble formation occurs by significantly different mechanisms compared with those that are important in macroscale, unconfined flows (Stone 1994). Surface-active species such as surfactants and particles strongly influence the interfacial dynamics, with diffusion and adsorption-desorption kinetic timescales often comparable to microfluidic flow timescales.

The complexity of microfluidic geometries means that experiments drive many of the advancements in the field. Simulations and analysis are needed to provide important insight into mechanisms and access to variables that cannot be measured in experiments. Even at the low Reynolds numbers characteristic of microfluidic flows, resolving interfacial motion in conjunction with fluid flow in these geometries is computationally intensive and prone to numerical instability. Prior literature characterizing the breakup and motion of droplets and bubbles in pressure-driven flows in circular capillaries provides important fundamental underpinnings to the understanding of multiphase microfluidics (Olbricht 1996), but the noncircular channel cross sections that are common in microfluidics play a surprisingly important role in regulating the observed behavior.

The present review discusses each of the above aspects of the formation and motion of droplets and bubbles in microfluidic geometries, first focusing on mechanisms of formation when the interfacial tension is essentially uniform, then considering the influence of surface-active materials, and finally examining the critical role of the entire hydraulic network in regulating droplet and bubble production. The next section outlines the underlying fundamental parameters and governing equations for interfacial flows at the microscale.

2. TWO-PHASE FLOW IN MICROFLUIDIC GEOMETRIES

Droplets and bubbles are generated in a variety of planar microfluidic geometries designed to bring two or more immiscible fluid streams into contact with one another. The most common geometries

can be broadly categorized into three types (Christopher & Anna 2007): coflow geometries in which immiscible fluids meet in parallel streams; cross-flow geometries in which the immiscible fluid streams meet at an angle to one another; and flow-focusing geometries in which there is a geometric element that causes the streams to accelerate, narrowing the inner fluid thread. **Figure 1** shows the characteristic dimensions for each geometry, where w_i and w_o represent the widths of the upstream inlet channels for the dispersed and continuous phase liquids, respectively, and w represents the width of the downstream channel into which droplets are generated. All channels are planar with uniform depth h, and the width w_{or} represents the width of the orifice in the flow-focusing geometry. Analytical solutions are generally not possible given the complexity of these geometries and the presence of deformable fluid interfaces. Instead, experiments and numerical simulations focus on characterizing droplet production in terms of the controlling dimensionless parameters. Phenomenological models also help capture relevant behaviors that are important in the effective design of multiphase microfluidic devices.

The controlling dimensionless parameters in microfluidic droplet production include the capillary number, $Ca = \mu_o U/\gamma = \mu_o G a_0/\gamma$, the flow rate ratio $\varphi = Q_i/Q_o$, and the viscosity ratio $\lambda = \mu_i/\mu_o$. The dimensional variables defining these parameters are the volumetric flow rate Q, the viscosity μ, and the interfacial tension γ, and the subscripts i and o refer to the inner dispersed phase fluid and the outer continuous phase liquid, respectively. The characteristic velocity U appearing in the capillary number is defined differently for each geometry, sometimes in terms of a characteristic deformation rate G and droplet radius a_0. For example, the capillary number for both cross-flow and coflow geometries is typically defined in terms of the mean velocity of the outer fluid, $U = Q_o/wh$, where w and h are the width and depth of the downstream channel, respectively (Christopher et al. 2008, De Menech 2006, Glawdel et al. 2012a). The capillary number for flow-focusing geometries is defined in terms of the axial elongation rate in the flow-focusing nozzle,

$$G = \frac{Q_o}{h\Delta z}\left(\frac{1}{w_{or}} - \frac{1}{2w_o}\right), \tag{1}$$

where Δz is the axial distance between the end of the inlet channel for the dispersed phase and the flow-focusing orifice of width w_{or}. The width w_o is that of the inlet channel for the continuous phase (Lee et al. 2009). The characteristic droplet radius is given by the half width of the dispersed phase channel, $a_0 = w_i/2$. In many microfluidic flows, inertia can be neglected, and thus the Reynolds number, $Re = \rho U a_0/\mu$, and Weber number, $We = \rho U^2 a_0/\gamma$, are typically small in both fluid phases, where ρ is the fluid density.

In the absence of inertia, fluid flow in the inner and outer liquids is described by Stokes' equations and continuity,

$$\begin{aligned} \mu_i \nabla^2 \mathbf{v}_i &= \nabla p_i, \quad \nabla \cdot \mathbf{v}_i = 0, \\ \mu_o \nabla^2 \mathbf{v}_o &= \nabla p_o, \quad \nabla \cdot \mathbf{v}_o = 0, \end{aligned} \tag{2}$$

where $\mathbf{v}$ is the local fluid velocity, and p is the local fluid pressure. The deformable fluid-fluid interface couples the two phases by requiring continuity of velocity at the interface. In addition, the stress balance at the interface requires

$$\frac{\mu_o a_0 G}{RT\Gamma_\infty}\left(\underline{\underline{\mathbf{T}}}^o - \lambda\underline{\underline{\mathbf{T}}}^i\right)\cdot\mathbf{n} + \nabla_s\gamma - \gamma\mathbf{n}(\nabla_s\cdot\mathbf{n}) = 0, \tag{3}$$

where R is the ideal gas constant, T is temperature, Γ_∞ is the maximum surface concentration of the surfactant, $\underline{\underline{\mathbf{T}}}$ is the stress tensor in the bulk fluid evaluated at the interface, $\mathbf{n}$ is the unit normal vector to the interface, and ∇_s is a surface gradient operator (Stone & Leal 1990). The stress balance therefore includes interfacial tension gradients as well as the Laplace pressure jump

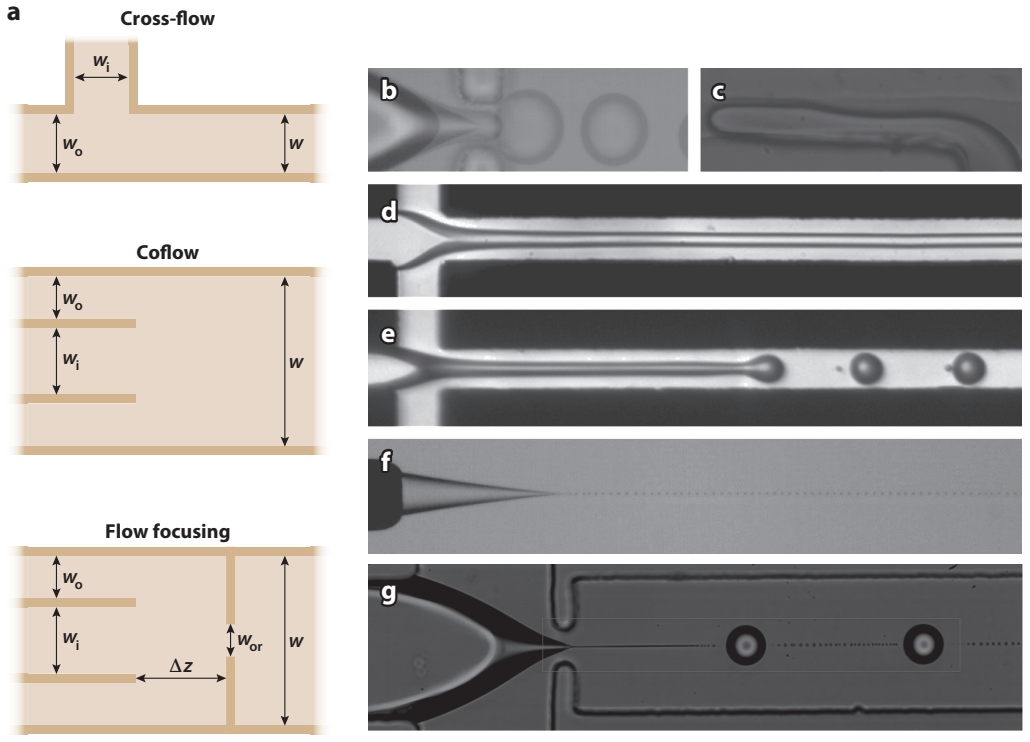

Figure 1

(*a*) Schematic diagrams of planar microfluidic droplet generators: cross-flow, coflow, and flow focusing. Planar dimensions are labeled, and the channel depths are uniform with depth *h*. (*b–g*) Images of typical droplet-generation modes: (*b*) squeezing mode of droplet breakup in a flow-focusing geometry, (*c*) squeezing mode of droplet breakup in a cross-flow geometry, (*d*) stable jet formation in a confined flow-focusing geometry, (*e*) dripping mode of jet breakup in a flow-focusing geometry, (*f*) extremely fine thread formation in coflow, and (*g*) tip streaming in a flow-focusing geometry. Typical channel dimensions in each case are of the order of 10–100 μm. Panel *b* reprinted with permission from Anna & Mayer (2006). Copyright 2006, AIP Publishing LLC. Panels *d* and *e* reprinted with permission from Cubaud & Mason (2008). Copyright 2008, AIP Publishing LLC. Panel *f* reprinted with permission from Gordillo et al. (2014). Panel *g* reprinted with permission from Lee et al. (2009). Copyright 2009, AIP Publishing LLC.

across a curved interface. Interfacial tension gradients are negligible when there are no surfactants present in an isothermal system.

When soluble surfactants are present, the surface-active species partitions to both the bulk and the interface, requiring the convection-diffusion equation to be satisfied, potentially in both liquid phases. A controlling dimensionless parameter for surfactant mass transport to interfaces is the Péclet number, $Pe = a_0^2 G/D$, describing the relative timescales for diffusion and convection, where D is the bulk diffusivity of the surfactant molecule. The flux of surfactant from the bulk to the interface, j_n, is described by serial processes of advection-diffusion and adsorption-desorption kinetics (Alvarez et al. 2011, Jin & Stebe 2007, Moyle et al. 2012, Stone & Leal 1990, Wang et al. 2014). The interfacial surfactant mass balance resulting from coupling of the flow and the mass

flux is given by

$$\frac{\partial \Gamma}{\partial t} + \nabla_s \cdot (\Gamma \mathbf{v}) + 2H\,(\mathbf{n} \cdot \mathbf{v})\Gamma - D_s \nabla_s^2 \Gamma = j_n, \tag{4}$$

where Γ is the interfacial concentration of surfactant, H is the mean interfacial curvature, $\mathbf{v}$ is the velocity at the interface, and D_s is the surface diffusivity. Upon normalizing the evolution equation by the maximum surface concentration and a characteristic timescale G^{-1} for interfacial deformation, a surface Péclet number $Pe_s = a_0^2 G / D_s$ arises in the final term on the left-hand side of Equation 4. Finally, the interfacial tension γ is connected to the interfacial concentration of surfactant Γ through a surface equation of state whose form is determined by the isotherm model selected (Chang & Franses 1995, Eastoe & Dalton 2000). Even the simplest models that capture realistic isotherm, equation of state, and kinetic behaviors are nonlinear, so interfacial flow problems involve strongly coupled and nonlinear processes of fluid flow, mass transport, and interfacial deformation.

Interfacial flow problems such as those found in multiphase microfluidics are challenging to model numerically given the need to track interfaces that are deforming and changing their interfacial area and topology (e.g., through pinch-off and coalescence). When surfactants are present, species concentrations in the bulk and on the interface must also be tracked. Multiphase microfluidics problems have motivated the further development of numerical methods for these situations, especially those that can incorporate soluble surfactants. Numerous approaches have been developed with a goal of achieving numerical stability and high accuracy over a wide range of length scales and timescales. Highly resolved finite element schemes track the trajectory, shape, and local surface concentration at sharp interfaces (Ganesan & Tobiska 2012). Phase-field methods resolve the diffuse interface structure using a free energy functional to evolve two order parameters, one describing the oil-water interface and the other describing the surfactant volume fraction (Liu & Zhang 2010, van der Sman & van der Graaf 2006). Boundary integral methods address free-surface Stokes flows and readily include insoluble surfactants, which are restricted to the interface (Bazhlekov et al. 2006, Eggleton & Stebe 1998). When the transport of soluble surfactants is involved, surfactant concentration gradients must be accurately resolved to properly couple the bulk transport with the surfactant evolution on the interface. This is particularly challenging at high Péclet numbers at which the length scale of the gradient is very small. A hybrid method using a perturbation analysis of the thin depletion layer near the interface is able to accurately resolve surfactant dynamics in problems involving the deformation and breakup of droplets in the presence of soluble surfactants at high Péclet numbers (Booty & Siegel 2010).

3. DROPLET AND BUBBLE FORMATION WITH UNIFORM INTERFACIAL TENSION

Microfluidic geometries for droplet and bubble generation, and the accompanying flow fields, can vary considerably. However, the mechanisms for droplet and bubble breakup are similar for a wide range of geometries. Breakup mechanisms have been examined in detail in experiments, simulations, and analyses and can be divided into several regimes. It is quite common in microfluidics to assume constant interfacial tension even when surfactants are present in the system. This section discusses regimes of droplet and bubble production in which the assumption of uniform interfacial tension is valid; typically, this is true not only in the absence of surfactant, but also at very high surfactant loading, where the interfacial tension is taken to be the equilibrium value for the relevant bulk concentration.

Two central themes in microfluidic droplet production are that confinement plays a critical role in the deformation and breakup of the fluid interface at all flow conditions and that the 3D

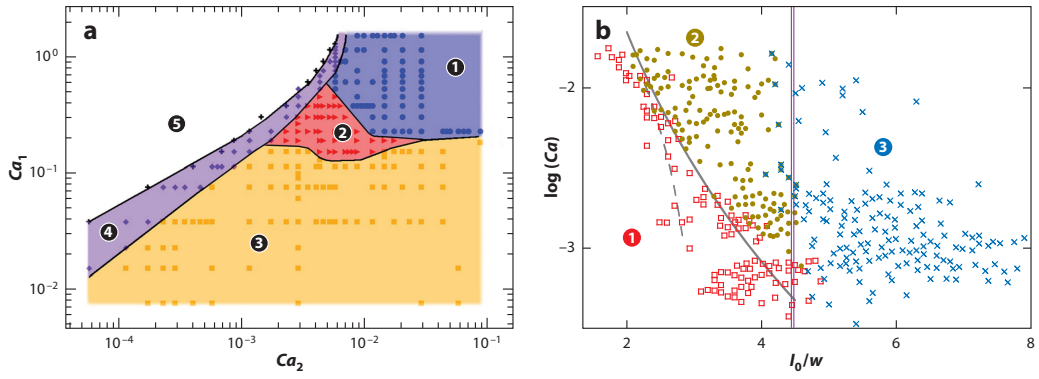

Figure 2

Examples of operating diagrams depicting conditions at which various droplet breakup modes occur. (*a*) Flow-focusing breakup in terms of the capillary numbers of the inside (Ca_1) and outside (Ca_2) phases. Regions ❶,❹, and ❺ represent different types of stable thread formation; region ❷ represents a jetting mode; and region ❸ represents squeezing mode breakup. Panel *a* adapted with permission from Cubaud & Mason (2008). Copyright 2008, AIP Publishing LLC. (*b*) Splitting droplets at a bifurcating junction as a function of the capillary number and initial length of the incident droplet. In region ❶, droplets do not break up; in region ❷, droplets break up with partial obstruction of the channel; and in region ❸, droplets break up with full obstruction of the channel. The solid gray line represents the stability curve predicted by Leshansky & Pismen (2009), and the dashed line represents the stability curve predicted by Link et al. (2004). The double purple vertical line represents the critical dimensionless droplet length above which full obstruction of the channel is predicted based on geometric arguments of Jullien et al. (2009). Panel *b* adapted with permission from Jullien et al. (2009). Copyright 2009, AIP Publishing LLC.

flow in rectangular microchannels is surprisingly important in regulating the local velocity and pressure fields near the deforming interface. At very low capillary numbers, droplets and bubbles are generated by a squeezing mode of breakup characterized by the obstruction of the continuous phase liquid by the growing interface and by the quasi-stable pinch-off of the neck (**Figure 1*b*,*c***). At larger capillary numbers, fluid threads form that can break up by absolute (dripping) or convective (jetting) instabilities, modulated by the confinement of the thread within the downstream channel (**Figure 1*d*,*e***). At intermediate capillary numbers, viscous stresses play a role in the deformation of the fluid interface during droplet formation, modifying the resulting droplet sizes. These regimes are mapped as a function of flow parameters in **Figure 2*a*** for cross-channel flow-focusing devices (Cubaud & Mason 2008); similar maps can be generated for other geometries.

3.1. Squeezing Mode of Droplet and Bubble Production

At low capillary numbers, $Ca < 0.01$, viscous stresses are not sufficient to overcome the confining effects of the microchannel walls, and the geometry plays a leading role in the formation of bubbles and droplets. Microscopic observations in both T-shaped junctions (Garstecki et al. 2006) and flow-focusing geometries (Garstecki et al. 2004) demonstrate that the emerging liquid or gas interface grows until it obstructs the junction region, or the contracting region in a flow-focusing device. Once the interface fully obstructs the channel, the interface narrows until a bubble or droplet pinches off.

Measurements of the local pressure variations in both the dispersed and continuous phase fluid streams were achieved using Laplace pressure sensors in which an immiscible interface of a sensor fluid is in contact with the fluid streams of interest. Variations in the curvature of the sensor

interface indicate the local pressure through the Laplace equation, $p_1 - p_2 = 2\gamma / a_s$, where p_1 is the pressure in the test fluid, p_2 is the constant pressure in the sensor fluid, γ is the interfacial tension between sensor and test fluids, and a_s is the radius of curvature of the sensor interface (Abate et al. 2012, Romero & Abate 2012). In both T-junction and flow-focusing geometries, the pressure in the continuous phase liquid upstream of the emerging droplet rises sharply as the droplet obstructs the downstream channel. As the neck pinches off, the continuous phase pressure exhibits a maximum and decreases. The pressure in the dispersed phase liquid decreases and then increases out of phase with the continuous phase pressure, while the downstream pressure remains relatively flat (see **Figure 3*a***). The maximum pressure variation in each phase decreases with the capillary number, with the two pressures becoming more comparable as the capillary number increases.

These observations lead to a scaling analysis of the size of the emerging bubble or droplet. The growth rate of the initial emerging interface is proportional to the velocity of the inner fluid stream. The large pressure generated upstream pushes the interface toward the pinch-off location, causing it to narrow at a rate proportional to the velocity of the outer phase liquid. Thus, the bubble length L_b is expected to be linearly proportional to the flow rate ratio φ and the width of the channel w,

$$L_b / w = A_1 + A_2 \varphi. \quad (5)$$

Experiments generally agree with the expected scaling, but the coefficients A_1 and A_2 must be fitted and vary with the cross-sectional geometry of the pinch-off region (Garstecki et al. 2006, Jensen et al. 2006).

Micro-particle image velocimetry (micro-PIV) measurements of the velocity field surrounding the emerging interface reveal that the 3D flow in the rectangular microchannels plays a critical role, beyond what can be deduced from 2D projections of the interface deformation. The gutters that form in the corners of the rectangular cross section allow a significant fraction of the continuous phase liquid to leak around the emerging interface even when complete obstruction is apparent in the top-down view (van Steijn et al. 2007, 2009). Thus, the fluid has a pathway by which to flow around the emerging drop. Recognizing the importance of the 3D shapes of droplets and bubbles confined within microchannels has led to improved methods to estimate these shapes from 2D projections (Musterd et al. 2015).

The velocities measured in the corner gutter regions are up to 10 times faster than predicted for bubbles in polygonal channels (Wong et al. 1995a,b). Counter to expectations, the bubble speed increases with the bubble length. This is attributed to the rearrangement of the fluid interface to minimize resistance to flow, possibly through lateral drainage of fluid from the thin films into the gutters (de Lózar et al. 2008; van Steijn et al. 2007, 2009). Independent measurements of bubble and droplet velocities in rectangular microchannels also show significant deviations from the predictions of Wong et al. (Jakiela et al. 2011). The velocity depends strongly on the viscosity ratio and droplet length, and if the viscosity ratio is greater than 1, the velocity also depends strongly on the capillary number. For a long droplet that is less viscous than the surrounding liquid, the velocity is nearly equal to the superficial velocity of the continuous phase liquid. These measurements also show that the length of a flowing droplet is significantly longer than its static length, again indicating a rearrangement of the fluid interface to reduce resistance to flow.

The breakup mechanism in the late stages of bubble formation in the squeezing regime has been debated. Early arguments centered on classic capillary stability mechanisms (Dollet et al. 2008). However, strong confinement has been found to completely suppress capillary instabilities (Janssen et al. 2012). Comparisons of experimental interface shapes with static interface shapes during pinch-off show that the interface narrows quasi-statically until the very late stages of

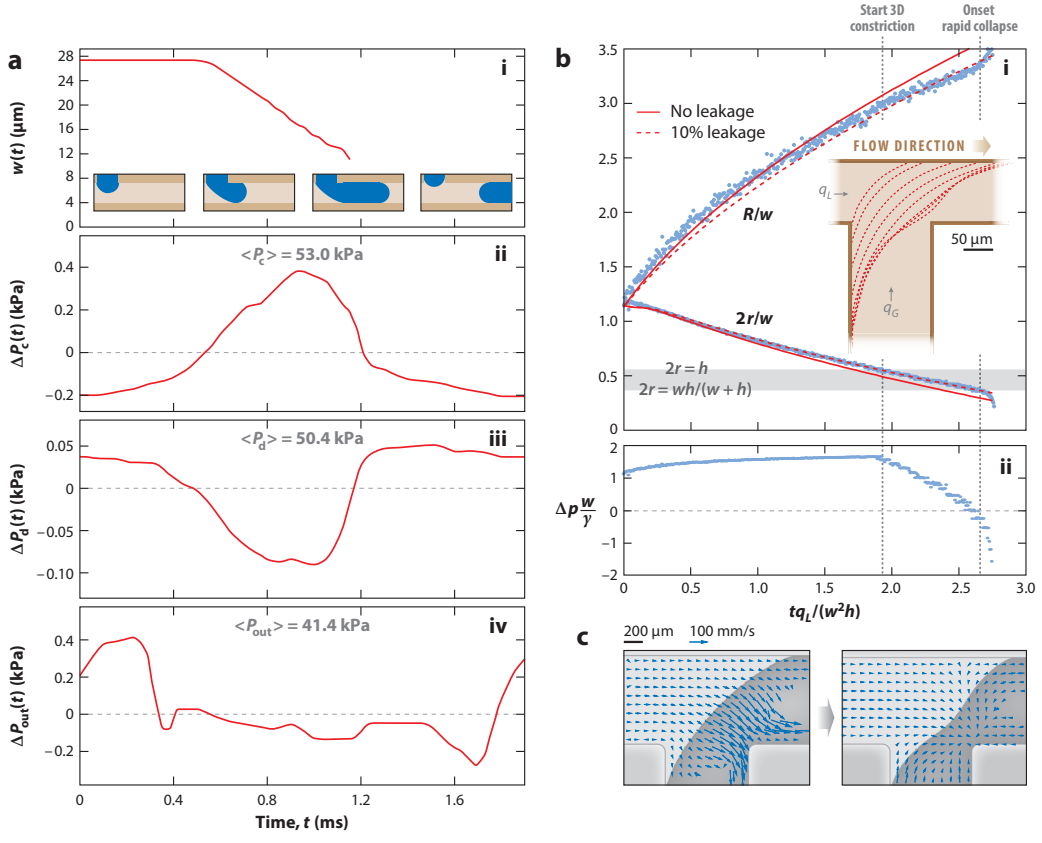

Figure 3

Pressure variations during squeezing mode breakup of droplets in cross-flow geometries. (*a*) Overall pressure variations in the continuous and dispersed phase liquids and the downstream channel as the neck thins. Panel *a* adapted from Abate et al. (2012) with permission of The Royal Society of Chemistry. (*b*,*i*) Local interface curvature variations and (*ii*) the local pressure drop along the gutters deduced from the interface curvature. (*c*) The local velocity field in the gutter region near the thinning neck obtained from micro-particle image velocimetry measurements. Panels *b* and *c* adapted from van Steijn et al. (2009). Copyright 2009 by the American Physical Society.

breakup, when rapid thinning and collapse of the thread ensue (Garstecki et al. 2005). Micro-PIV measurements and estimates of the local interface curvature of the emerging bubble reveal the onset of an adverse pressure gradient just prior to rapid neck collapse (**Figure 3*b*,*c***), which drives a reversal of the flow in the corner gutter regions, precipitating catastrophic neck collapse (Funfschilling et al. 2009, van Steijn et al. 2009). The cross-sectional dimensions of the downstream channel determine the critical thread radius for flow reversal and rapid neck collapse, $r_{crit} = hw / [2(w + h)]$, where h is the depth of the channel (van Steijn et al. 2009). These observations suggest that the pinch-off of a fluid thread in the squeezing regime is never driven by a capillary instability.

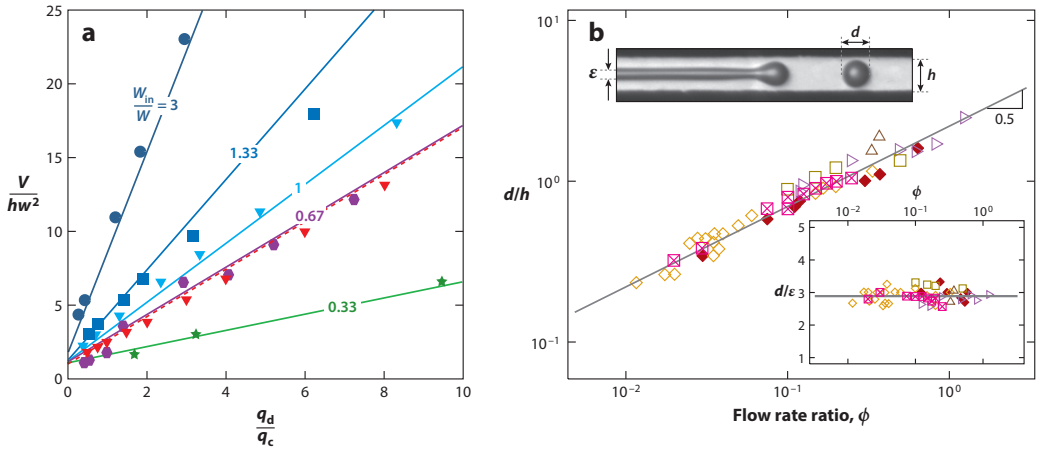

Figure 4

Scaling of droplet size with experimental parameters in (*a*) squeezing mode of breakup in a cross-flow geometry and (*b*) jetting mode of breakup in a flow-focusing geometry. In panel *a*, the droplet volume depends primarily on the flow rate ratio and the channel aspect ratio. The symbols indicate experiments, compared with a model prediction of van Steijn et al. (2010) indicated by the corresponding solid lines for gas-liquid pairs; the dashed red line and corresponding red triangles indicate model and experiments for liquid-liquid pairs. In panel *b*, the droplet diameter scales with the square root of the flow rate ratio, as expected for the primary pressure-driven flow of coflowing streams. Symbol shapes in panel *b* indicate experiments conducted with different fluid pairs, resulting in different viscosities, viscosity ratios, and surface tensions. Panel *a* adapted from van Steijn et al. (2010) with permission of The Royal Society of Chemistry. Panel *b* adapted with permission from Cubaud & Mason (2008). Copyright 2008, AIP Publishing LLC.

van Steijn et al. (2010) incorporated these detailed observations of the local velocity and pressure fields into a closed-form model describing squeezing flow breakup. The droplet volume V is given by the expression

$$\frac{V}{bw^2} = \frac{V_{\text{fill}}}{bw^2} + \alpha\varphi, \tag{6}$$

where V_{fill} is a function solely of the geometry of the T-junction, and α depends on geometry and the fraction of flow allowed to leak through the corner gutters. Equation 6 is consistent with the early scaling arguments represented by Equation 5 but incorporates the role of geometry and 3D flow without the need for fitting parameters. **Figure 4*a*** compares measured droplet volumes with this model for several channel geometries.

The squeezing mechanism also controls other droplet processes in microfluidic devices. For example, when a pre-formed droplet collides with a T-shaped junction, it will either split into two segments or travel into one of the arms of the T, depending on the impact speed and the initial length of the drop (Link et al. 2004). The hydraulic resistances in the branches of the T determine the relative volumes of the resulting segments when breakup occurs (Link et al. 2004) and the branch selected when breakup does not occur (Belloul et al. 2009, Choi et al. 2011, Glawdel et al. 2011, Parthiban & Khan 2012). Assuming 2D flow in the T-junction, a lubrication analysis is used to estimate the squeezing pressure acting on the droplet within the junction, driving thinning and stretching. Combined with a geometric construction of the quasi-steady interface shape, this analysis predicts a power law relationship between the critical capillary number for droplet breakup

and the initial extension ε of the drop, given by

$$\varepsilon \equiv L_0 / w \approx \chi Ca^{-0.21}, \tag{7}$$

where L_0 is the initial droplet length, w is the width of the impinging channel, and χ is a constant coefficient that depends on the dimensionality ($\chi \approx 0.98$ for 2D geometries) (Leshansky & Pismen 2009). Numerical simulations confirm and extend these arguments for different viscosity ratios (Afkhami et al. 2011) and show that the flow in the corner gutter regions is negligible, validating the 2D assumption (Hoang et al. 2013). Experiments conducted for a wide range of capillary numbers, $4 \times 10^{-4} < Ca < 0.2$, and two different viscosity ratios also demonstrate excellent agreement with the squeezing analysis, as long as there is a small gap between the extending drop and the downstream walls of the microchannel, permitting flow around the drop (Jullien et al. 2009). Beyond a critical length, the extending drop fully obstructs the downstream arms, a small gap never forms, and breakup always occurs regardless of the capillary number. Notably, although the squeezing arguments are formally valid for $Ca^{1/5} \ll 1$, the scaling given in Equation 7 agrees well with experiments for significantly larger capillary number values. By contrast, early arguments centering on classic capillary stability arguments (Link et al. 2004) fail to agree with experiments except in a very narrow region at moderately large capillary number values (**Figure 2*b***).

As the capillary number increases, viscous stresses are sufficient to deform the emerging fluid interface, impacting the size and frequency of the resulting droplets. In this case, experiments (Christopher et al. 2008, Glawdel et al. 2012a, Nie et al. 2008) and numerical simulations (De Menech et al. 2008, Gupta & Kumar 2010, Jensen et al. 2006) show that the droplet size depends on the capillary number and viscosity ratio in addition to the flow rate ratio and geometry. However, the squeezing mechanism remains operational at all Ca, φ, and λ (De Menech et al. 2008). Measurements of pressure oscillations in the dispersed and continuous phase streams show that although fluctuations decrease, they persist well into the regime in which viscous stresses are important, indicating that droplet breakup never transitions to fully viscous-dominated breakup (Abate et al. 2012, Romero & Abate 2012). Models developed to describe the transition regime when both squeezing and viscous stresses are relevant have achieved mixed success (Christopher et al. 2008; Glawdel et al. 2012b; Husny & Cooper-White 2006; Sang et al. 2009; Steegmans et al. 2009a,b). These models typically build on the multistage process of filling, pushing, and rapid neck collapse observed in the squeezing limit but also include estimates of viscous deformation of the emerging fluid interface. Generally, these models estimate the squeezing pressure and the viscous force on the interface and result in droplet volume estimates similar in form to Equation 6. The coefficients α and V_{fill} are replaced by functions of the capillary number, viscosity ratio, and channel geometry (Christopher et al. 2008) and may also include an initial lag phase in which the interface recovers after detachment (Glawdel et al. 2012b).

3.2. Dripping and Jetting of Fluid Threads

At large capillary numbers, $Ca > 0.1$, the fluid interface does not break as readily, and coflowing fluid threads form, regardless of the details of the microfluidic geometry. The thread diameter d_t scales with the flow rate ratio as

$$d_t \sim \varphi^{1/2}, \tag{8}$$

consistent with analysis of the primary pressure-driven flow of two fluid streams in the absence of capillary effects (**Figure 4*b***) (Castro-Hernández et al. 2012, Cubaud & Mason 2008, Humphry et al. 2009, van Hoeve et al. 2010). Confinement within the microchannel delays breakup of the thread compared with classic stability theory for viscous and inviscid jets (Cubaud & Mason 2008,

Rayleigh 1879, Tomotika 1935). When the thread radius is larger than the depth of the channel, the instability is completely suppressed (Humphry et al. 2009, Janssen et al. 2012). Combined with the scaling of the thread radius given in Equation 8, this condition leads to a criterion for complete suppression of thread breakup (Humphry et al. 2009), given by

$$(w/h)(Q_i/Q_o)(\mu_i/\mu_o) > 1. \tag{9}$$

Less confined threads are always unstable (Janssen et al. 2012), but breakup is delayed because of the presence of nearby walls (Gañán-Calvo 2008; Guillot et al. 2007, 2008; Herrada et al. 2008). Numerical analysis reveals that interface shape perturbations grow much more slowly in the direction perpendicular to the direction of confinement, ultimately leading to a noncircular thread cross-sectional shape and slowing the growth rate of the instability. The wave number corresponding to the maximum growth rate depends on the viscosity ratio and confinement ratio (Janssen et al. 2012).

In the presence of flow, confined fluid threads break via either dripping or jetting mechanisms (Humphry et al. 2009). Dripping, characterized by a narrowing thread, results in more uniform droplets and occurs when the thread undergoes an absolute instability with a stationary breakup location. Jetting, characterized by a widening thread, leads to less uniform droplets and occurs when the instability is convected along the thread (Utada et al. 2007, 2008). The transition from dripping to jetting depends on the capillary number of the outer fluid and the Weber number of the inner fluid. Narrowing threads occur when the dominant forces are viscous and capillary forces; widening jets occur when inertia and capillary forces are dominant (Utada et al. 2007). For widening jets, breakup occurs downstream of the nozzle at a position L_c that depends on geometry, flow rates, and fluid properties (Cubaud & Mason 2008),

$$L_c \sim \frac{\mu_i}{\gamma}(Q_i Q_o)^{1/2}, \tag{10}$$

where the proportionality constant depends on the cross-sectional dimensions w and h. Humphry et al. (2009) used these arguments for the location of thread breakup to design step changes in the channel depth, inducing thread breakup at a specific location along the channel axis. The resulting 2.5D device is reminiscent of step emulsification designs and may provide insight into the high degree of monodispersity of droplets formed in these methods (Priest et al. 2006, Shui et al. 2011, Stoffel et al. 2012).

In the narrowing jet regime, viscous stresses can be so significant that extremely narrow fluid threads form (**Figure 1*f***), producing droplets that are 1 to 30 μm in diameter, up to 100-fold smaller than the radius of the inner fluid channel (Gordillo et al. 2014, Marín et al. 2009). Extremely narrow threads occur in the absence of inertia, $Re_o \ll 1$ and $Re_i \sim O(1)$, surfactants, and electric fields and at conditions in which the outer viscous stresses dominate compared with the inner viscous stresses, $\varphi \ll 1$, $\lambda \ll 1$, and $Ca \sim O(1)$ (Gordillo et al. 2014). The diameter d_t of the narrow thread scales similarly to that of larger coaxial fluid threads, $d_t/d_c \sim (Q_i/U_o d_c^2)^{1/2}$, with d_c representing the inner capillary diameter, and U_o the average outer fluid velocity (Marín et al. 2009).

The formation of extremely narrow threads coincides with the generation of a strong, radially inward velocity component just downstream of the end of the inner capillary, where the dispersed phase stream emerges (Suryo & Basaran 2006). The radially inward velocity field generates an axial velocity gradient, and the resulting extensional stresses focus and stretch the thread, suppressing the capillary instability until the axial velocity gradient diminishes downstream (Marín et al. 2009, Suryo & Basaran 2006). Stability analysis confirms that monodisperse droplet production corresponds to globally stable thin jets, which is achieved when the capillary number exceeds a threshold

value $1 < Ca_{crit} < 2$ depending on the viscosity ratio (Gordillo et al. 2014). This focusing mechanism resembles other instances in which fluid streams are focused to produce extremely small droplets (Anna & Mayer 2006, Blanchette & Zhang 2009, Gañán-Calvo et al. 2007, Gopalan & Katz 2010, Herrada et al. 2011). Tseng & Prosperetti (2015) unified these observations, arguing that each of these scenarios corresponds to a generic instability that occurs when local streamlines converge in the neighborhood of an interface. When flow is swept toward points at which the vorticity tangent to an interface vanishes, the interface is compressed. If surface tension is not sufficient to overcome the compression of the interface, perturbations grow, and a fluid filament is drawn from the convergence point.

In summary, microfluidic generation of droplets and bubbles is entirely different from the generation of droplets and bubbles in unconfined geometries (Stone 1994). Although viscous stresses and inertia can still play important roles, the confinement of the fluid interface is the controlling factor across a wide range of flow rates and geometries. In most cases, the 3D nature of the flow cannot be neglected. Interfacial instabilities other than classic capillary instabilities drive the evolution of the interface shape and the formation of droplets and bubbles. The predominantly quasi-static interfacial breakup mechanisms in confined geometries lead to the production of extremely uniform droplet and bubble sizes, largely eliminating the formation of satellite droplets that are notoriously difficult to suppress in unconfined breakup of fluid jets (Eggers & Villermaux 2008).

4. SURFACTANT EFFECTS ON DROPLET FORMATION

Surfactants are used extensively in multiphase microfluidic applications. Often, surfactant is added to stabilize bubbles and droplets against coalescence, and the amount of surfactant added to the system far exceeds the amount needed to fully saturate the interface. Surfactants are beneficial in several ways, lowering interfacial tension, maintaining desired wetting conditions at the channel walls, and hindering the coalescence of closely spaced droplets and bubbles. Surfactants can also interact with species in the bulk liquid phases and regulate transport across the interface. New surfactants have been designed specifically for microfluidic applications encapsulating cells or biomolecules in droplets. In these applications, there is a need for the inner surface of the droplet to be biologically inert, while providing stability of concentrated emulsions for long-term storage. Successful examples of surfactants designed with these two goals in mind include block copolymer surfactants of oligomeric perfluorinated polyethers linked with polyethylene glycol (Holtze et al. 2008) or perfluoroalkyl tails with crown ethers or hexaethylene glycol head groups (Holt et al. 2010).

Beyond their primary role as stabilizers, surfactants also influence interfacial dynamics by coupling the interface deformation with the bulk fluid flow. The most interesting behaviors are observed at intermediate concentrations, at which timescales for flow compete with timescales for transport, including diffusion, adsorption, and desorption, and the development of interfacial tension gradients. Microfluidic length scales provide access to new regions of parameter space because the characteristic timescale for diffusion to curved interfaces is shorter (Alvarez et al. 2010, Jin et al. 2004) and flow speeds are faster. As a result, interfacial transport in many microfluidic applications is kinetically limited, and Marangoni stresses are significant. Typically, interfacial fluid dynamics in microfluidic devices occurs at low Reynolds numbers, moderate capillary numbers, and high Péclet numbers (Wang et al. 2014).

Surfactants alter the dynamics of droplet breakup and coalescence. For rapid droplet production, a new interface may be generated too quickly for the surfactant to fully populate the interface. The observed variation in droplet size in the presence of slowly adsorbing surfactant can be explained by the larger interfacial tension of the nonequilibrated interface (Wang et al. 2009,

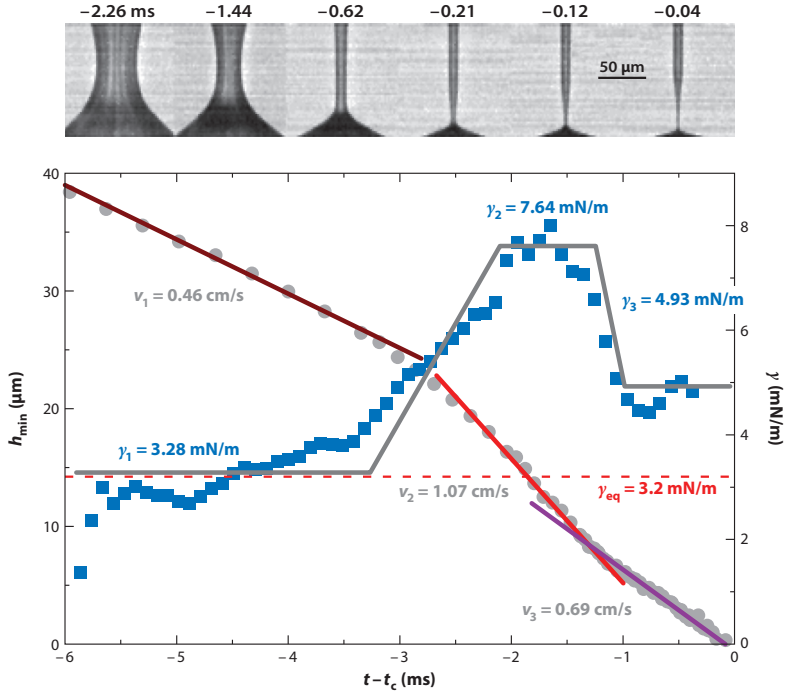

Figure 5

Three stages of linear thinning of fluid threads in a flow-focusing geometry in the presence of surfactants. Figure adapted with permission from Roché et al. (2009). Copyright 2009 by the American Physical Society.

J.H. Xu et al. 2012). Similarly, droplets whose interfaces are well below equilibrium surfactant coverage merge rapidly with fully saturated droplets, whereas droplets containing more than a threshold value of surface coverage do not merge (Baret et al. 2009, Mazutis & Griffiths 2012, Mazutis et al. 2009). During pinch-off of a droplet, several stages of linear neck thinning (see **Figure 5**) are observed that are uniquely attributed to the presence of surfactants (Roché et al. 2009). In the first stage, the slope of the linearly thinning neck radius corresponds to that of viscocapillary thinning (Papageorgiou 1995), using the equilibrium interfacial tension. The second stage exhibits a steeper slope arising from the depletion of surfactant in the thin neck region as well as non-negligible inertia (Eggers 1993). Notably, the depletion of surfactant can occur even if the bulk concentration is greater than the critical micelle concentration, given the very small length scales and timescales involved. The third-stage dynamics are slower again, as a result of nonmonotonic variation of surface tension along the filament. In this case, Marangoni stresses drive the surfactant toward the pinch-off location, as has been observed in other droplet breakup studies (Jin et al. 2006, Park et al. 2013, Young et al. 2009). The resulting dynamics of thinning is slowed because of the lower capillary pressure in the thread, which reduces the pressure gradient driving pinch-off. The surfactant solubility mitigates the effect by permitting desorption from highly concentrated regions (Young et al. 2009).

Surfactant also impacts the motion and deformation of droplets in microfluidic geometries. The deformation of surfactant-covered droplets in converging-diverging geometries has been used to determine the dynamic interfacial tension (Martin & Hudson 2009). In relatively unconfined geometries, droplets migrate laterally toward the centerline of a unidirectional pressure-driven flow owing to Marangoni stresses along the droplet surface. Furthermore, surfactants collect at the tips of deformed drops, which promotes tip stretching because of lower interfacial tension, which further enhances lateral migration (Janssen & Anderson 2008). Lateral migration also occurs when the interfacial rheology is more complicated. For example, dilatational interfacial stresses strongly impact droplet migration, even more dramatically than interfacial shear stresses do (Schwalbe et al. 2011). For confined droplet slugs in rectangular channels, droplet speeds at high and low surfactant concentrations are comparable to the average velocity of the surrounding liquid. At intermediate concentrations, the slug speed is significantly lower as a result of a surface concentration gradient that develops along the slug body. The faster surrounding fluid sweeps the surfactant from the trailing end to the leading end of the bubble. The resulting Marangoni stress drives fluid flow through the corner gutters and slows the overall axial speed of the slug itself (Fuerstman et al. 2007).

The interplay of surfactant transport and flow plays a critical role in the phenomenon of surfactant-mediated tip streaming. Tip streaming occurs most readily in a flow-focusing droplet generator, in which strong accelerating flow sweeps the surfactant along the interface toward the emerging tip. Surfactants that desorb slowly cannot easily escape the highly concentrated tip region, leading to a dramatic reduction of the interfacial tension there. A thin fluid thread is drawn from the nearly conical interface and breaks into droplets significantly smaller than the nozzle (**Figure 1*g***) (Anna & Mayer 2006, Lee et al. 2009). Droplets can be as small as 200 nm in diameter depending on the flow and surfactant conditions (Jeong et al. 2012, Moyle et al. 2012). Tip streaming occurs in flow-focusing devices at intermediate surfactant concentrations and capillary numbers $0.4 < Ca < 1.0$ but is suppressed at the extremes of the concentration and flow rate. These conditions are consistent with those found for tip streaming of unbounded droplets (de Bruijn 1993, Taylor 1934). Microfluidic tip streaming is enhanced by maintaining a relatively low flow rate ratio, $\varphi < 1/40$, and a relatively low viscosity ratio, $\lambda < 10$ (Anna & Mayer 2006, Lee et al. 2009). Tip streaming can be periodic or sustained in flow-focusing devices depending on the rate of supply of surfactant to the interface compared with its removal during the tip streaming process (Jeong et al. 2012, Moyle et al. 2013).

The ejection of a thin thread from the tip of a conical interface is consistent with the stability arguments of Tseng & Prosperetti (2015) when local streamlines converge near an interface. The high surfactant concentration at the tip weakens the ability for interfacial tension to suppress the instability, making the phenomenon more robust. However, tip streaming does not occur at all conditions. At high and low concentrations and flow rates, tip streaming is suppressed, and squeezing, dripping, or jetting is observed. In light of the stability arguments, tip streaming is suppressed when the high tip concentrations cannot be maintained.

Surfactant mass transport controls whether high tip concentrations can be maintained and tip streaming can occur at a given set of conditions. A surface tension gradient is needed to counteract the radially converging fluid velocity to maintain a steady conical interface shape and is estimated by

$$\gamma - \gamma_0 = -\frac{3(\mu_o - \mu_i) Q_o \sin\theta_c \cos\theta_c}{w_{or} b(3\cos^2\theta_c - 1)} \left(\frac{r_c^2}{r^2}\right)\left(1 - \frac{r^2}{S^2}\right), \tag{11}$$

where γ_0 is the interfacial tension in the absence of surfactant, θ_c is the cone semiangle, w_{or} is the width of the flow-focusing orifice, r is the radial distance from the tip of the cone, S is the length of

the conical interface, and r_c is the radial distance from the tip to the location at which the thread connects with the cone. Integrating over the surface concentration profile $\Gamma(r)$ corresponding to Equation 11 provides an estimate of the total mass of surfactant needed to bring about tip streaming,

$$N_{\text{cone}} = 2\pi \int_{r_c}^{S} \Gamma(r)\, r \sin\theta_c dr. \tag{12}$$

The rapid formation of fresh interface combined with rapid diffusion at high bulk concentrations (Anna & Mayer 2006, Lee et al. 2009) suggests that surfactant adsorption barriers are rate limiting for interfacial transport. Estimating the amount of surfactant adsorbed at short times, one obtains

$$N_{\text{ads}} \approx \beta C_\infty \Gamma_\infty \tau_d (\pi w_i^2/2), \tag{13}$$

where C_∞ is the bulk surfactant concentration, Γ_∞ is the maximum surface concentration, and w_i is the width of the inlet stream channel. The timescale τ_d for droplet breakup,

$$\tau_d \approx \frac{0.15 d_H^3}{Q_i Ca}, \tag{14}$$

has been described semiempirically (Lee et al. 2009) and is given in terms of the hydraulic diameter of the flow-focusing orifice, $d_H = 2w_{or}h/(w_{or}+h)$. The adsorption rate constant β for the surfactant-oil-water system can be independently characterized (Alvarez et al. 2011). Combining Equations 12 and 13 provides a criterion for the onset of tip streaming, which, when combined with other geometric and global mass balance constraints, leads to predicted boundaries for tip streaming that coincide with the observed boundaries (**Figure 6*a***) (Moyle et al. 2012). Similar boundaries are also predicted in numerical simulations using a hybrid boundary integral method for high–Péclet number flows (**Figure 6*b***) (Wang et al. 2014). In both panels of **Figure 6**, the parameter space is represented by a dimensionless flow rate $\overline{Q} = \mu_o U_i / RT\,\Gamma_\infty$ along the horizontal axis and a dimensionless bulk concentration $\overline{C} = \mu_o w_i \beta C_\infty / 2RT\,\Gamma_\infty$ along the vertical axis, where U_i is a characteristic velocity of the inner fluid stream and the two dimensionless parameters represent the relative timescales of adsorption, convection, droplet breakup, and development of surface tension gradients.

An asymptotic formula for the tip streaming thread radius, obtained by matching self-similar solutions in the conical region with a slender jet approximation for the thread, predicts a scaling of the thread radius r_t of

$$r_t \approx \sin\theta_c (\gamma_{\min}/\gamma_{\max}) l_c, \tag{15}$$

where $l_c = \sqrt{\gamma_{\max}/\rho_i g}$ is the capillary length, g is the acceleration due to gravity, and $\gamma_{\max}$ and $\gamma_{\min}$ are the extreme values of the interfacial tension permitted along the interface (Krechetnikov 2012). The cone semi-angle depends most strongly on the nozzle geometry and weakly depends on the flow conditions (Lee et al. 2009). Therefore, the scaling analysis suggests that the most important factor in determining the tip streaming droplet size is the efficacy of the surfactant in lowering the interfacial tension (Ferri & Stebe 2000). To date, the scaling of the droplet size with conditions has not been determined experimentally.

Particles are also useful interfacial modifiers that can stabilize droplets and bubbles against coalescence (Pawar et al. 2011), arrest transport across interfaces (Abkarian et al. 2007, Pan et al. 2014), and impart unique interfacial mechanics (Brugarolas et al. 2014, Subramaniam et al. 2006, Wan & Stone 2012). Often, energy is required to drive particles to the interface, but once adsorbed, they remain pinned at the interface (Binks 2002). Microfluidic flows are well suited to the controlled loading of particles onto interfaces. Flow focusing has been used to collide micrometer-scale particles with a stationary bubble interface, capturing particles until the interface cannot resist

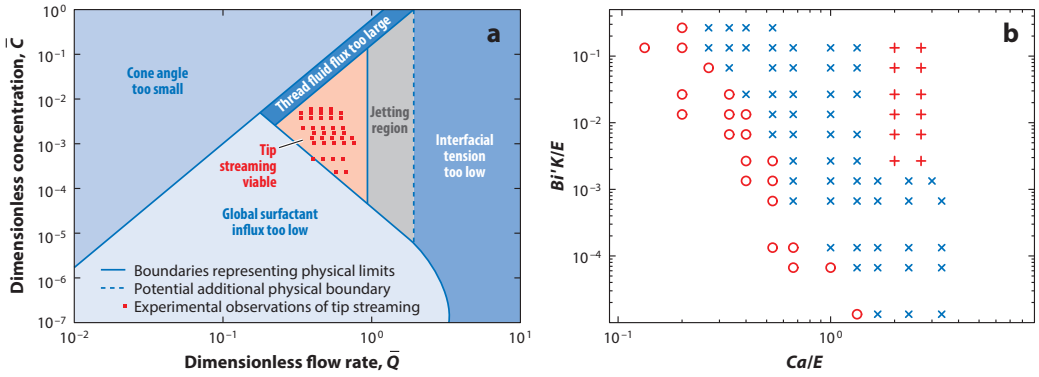

Figure 6

Comparison of operating conditions needed to achieve surfactant-mediated tip streaming as a function of the dimensionless surfactant concentration and dimensionless continuous phase flow rate, based on (*a*) experiments and predictions of a simplified transport model and (*b*) numerical simulations using a hybrid boundary integral method. Panel *a* adapted with permission from Moyle et al. (2012). Panel *b* adapted with permission from Wang et al. (2014). Copyright 2014, AIP Publishing LLC.

the upstream pressure and a jammed shell is ejected (Subramaniam et al. 2006). Bubbles flowing in nanoparticle suspensions along rectangular or circular microfluidic tubes also collect particles at the interface (Kotula & Anna 2012). The velocity difference between the droplet and the surrounding fluid sweeps particles to the trailing end, growing a jammed particle layer that eventually covers the entire surface and stabilizes the elongated droplet shape. The timescales for particle diffusion are comparable to the bubble residence times, allowing the residence time to be a controlling parameter for the particle coverage on a produced bubble or droplet (Kotula & Anna 2012, Priest et al. 2011). Particle-laden droplets and bubbles exhibit unique interfacial dynamics in microfluidic devices, including buckling and crumpling (Mulligan & Rothstein 2011), shape changes (Kotula & Anna 2012), and delayed coalescence (Priest et al. 2011). The relatively slow diffusion rates of particles compared with surfactants, and the large mechanical stresses that can be sustained by particle-laden interfaces, suggest the potential for further microfluidic applications involving droplets and bubbles with unique and controlled interfacial properties.

5. FEEDBACK EFFECTS IN MICROFLUIDIC NETWORKS

Aside from the local fluid and interfacial dynamics, the microfluidic network itself is also important to the formation of droplets and bubbles, which increase the hydraulic resistance of the channel in which they are flowing. Changes in the hydraulic resistance alter the local pressure within the interconnected channels of the overall microfluidic network. The number and length of bubbles in a channel segment, the interfacial tension (Adzima & Velankar 2006), and the presence of Marangoni stresses at moderate surfactant concentrations (Fuerstman et al. 2007) each impact the contribution of a bubble to the overall hydraulic resistance, in which the total pressure drop along a channel containing bubbles can be separated into contributions from the fluid segments between the bubbles, the bubble caps, and the bubble bodies (Fuerstman et al. 2007),

$$\Delta p_{\text{total}} = \Delta p_{\text{nb}} + \Delta p_{\text{body}} + \Delta p_{\text{caps}}. \quad (16)$$

Measured bubble velocities and dynamic lengths indicate that the interface rearranges to reduce hydraulic resistance (de Lózar et al. 2008, Jakiela et al. 2011, van Steijn et al. 2009). Existing quantitative descriptions of the hydraulic resistance as a function of bubble parameters and flow conditions are semiempirical or based on simplified models restricted to specific flow regimes. For example, Equation 16 can be written in terms of known parameters and semiempirical coefficients,

$$\Delta p_{\text{total}} = \frac{B_1 U_{\text{b}} \mu_{\text{o}}}{h^2}[A_0(L - L_{\text{b,tot}}) + B_2 L_{\text{body}} + B_3 nh(\mu_{\text{o}} U_{\text{b}} / \gamma)^{-1/3}], \tag{17}$$

where U_{b} is the bubble velocity, $A_0 = 12[1 - (192h/\pi^5 w)\tanh(\pi w/2h)]^{-1}$ is a geometric factor arising from the hydraulic resistance in a rectangular channel, L is the total length of the channel segment, $L_{\text{b,tot}}$ is the total length of all the bubbles in the segment, L_{body} is the total length of all the bubble bodies (between the end caps), and n is the number of bubbles in the segment. The dimensionless parameters B_1, B_2, and B_3 depend on factors such as the channel aspect ratio and flow in the gutters and are most easily determined empirically (Fuerstman et al. 2007).

The increased hydraulic resistance of the forming droplets impacts their generation even in a single microfluidic droplet generator. The effect is most pronounced in the formation of gas bubbles in flows driven by an applied pressure (Sullivan & Stone 2008). With an overall fixed pressure gradient along the channel, increased hydraulic resistance from bubbles downstream of the nozzle leads to a smaller pressure drop available for bubble generation at the nozzle, which in turn alters the size and frequency of formation. This leads to an initial transient in the bubble frequency as the downstream channel fills with bubbles and establishes a steady bubble distribution. The steady bubble generation frequency f_{SS}, incorporating the added downstream resistance, is given by

$$f_{\text{SS}} = \frac{Q_{\text{o}}(p_{\text{a}} - p_{\text{c}})}{\psi V_{\text{t}} p_a}, \tag{18}$$

where p_{a} is the applied pressure, and p_{c} is the pressure drop along the downstream channel containing only liquid. The volume V_{t} represents the volume of the gas thread and is given by the proportionality constant between the bubble volume and the applied pressure, $V_{\text{b}} = V_{\text{t}} p_{\text{a}} / p_{\text{c}}$. The constant ψ is an empirically determined constant that relates the pressure drop across a single bubble to the applied pressure, $\Delta p_{\text{b}} = \psi p_{\text{a}} V_{\text{t}} / V_{\text{c}}$, where $V_{\text{c}} = Lhw$ is the volume of the downstream channel. Equation 18 agrees well with experiments (Sullivan & Stone 2008). For flow rate-driven droplet generators, oscillations from the pumps can influence the polydispersity of produced bubbles (Korczyk et al. 2011). Compressibility of the dispersed phase fluid enhances both these effects.

Connecting multiple nozzles has clear utility for numbering up production of droplets and bubbles, as a single nozzle can at best produce on the order of 1 mL of bubbles or droplets per hour. Numbering up with multiple microfluidic nozzles is a desirable alternative to other methods such as microchannel emulsification (van Dijke et al. 2009) or step emulsification (Priest et al. 2006, Shui et al. 2011, Stoffel et al. 2012) because of the high degree of control of individual droplets and bubbles available in individual microfluidic nozzles. Multiple independent droplet generators feeding into a single outlet stream have been used to generate multicomponent emulsions and foams, with arbitrary control of bubble and droplet size and composition (Hashimoto et al. 2008, Li et al. 2008). The ability to generate arbitrary multicomponent, multiphase materials has potential application in a wide range of products and technologies, including foods, cosmetics, and drug delivery (Dickinson 2013, McClements 2012).

The influence of the microfluidic network is even more apparent when two or more droplet generators are connected together with common fluid supply inlets or common outlet collection channels. Changes in the hydraulic resistance of any segment containing bubbles or droplets

affect the entire network, including other droplet generator nozzles. Even with just two droplet generators having common inlets and outlets, droplet production can exhibit complex dynamics. The two generators can lock in to synchronized formation, or formation can be irregular or chaotic (Barbier et al. 2006). Separating the outlet collection streams significantly reduces the coupling between droplet generators, and further manipulating the outlet stream resistances offers even more control of the resulting polydispersity (Mulligan & Rothstein 2012).

Although separating outlet collection streams is feasible, using a common supply is important in a practical sense, reducing the number of external pumps needed. However, injecting fluid uniformly into multiple droplet generators can be a challenge. A viscous fluid finger propagating into a bifurcating channel will branch asymmetrically at high injection speeds if there is elasticity in the microfluidic network (Baroud et al. 2006) or at low injection speeds if there are diverging segments of the channel (Al-Housseiny et al. 2014). Scaling up further, different inlet branching geometries are sensitive to fabrication tolerances in different ways. For example, a tree structure with sequential, symmetric branches leading to 2^n inlet channels is nominally more energy efficient than a ladder structure with individual inlets branching from a main stream (Tetradis-Meris et al. 2009). However, the ladder is much less sensitive to small fabrication variations and produces more uniform emulsions with less variation in the output volume fraction. Several other larger-scale microfluidic networks have been designed for high-throughput emulsion production in microfluidics; these are reviewed in detail elsewhere (Vladisavljević et al. 2013).

Despite the complex dynamics, hydraulic circuit models capture all the behaviors described here for single and multiple nozzles, assuming an effective single-phase fluid resistance in each channel segment. The versatility of microfluidics also allows coupled processes to be decoupled using hydraulic resistance principles. By strategically placing bypass channels with relatively low fluidic resistance, regions of microfluidic networks can be isolated from one another. Low-resistance bypass channels have been used in both the oil and water streams to passively regulate and synchronize the formation and fusion of droplets in a pair of nozzles (Hong et al. 2010), in the droplet generator to regulate flow in the corner gutters and decouple squeezing breakup from the details of the incoming flow streams (van Steijn et al. 2013), and to control the timing of droplets entering a bifurcating junction (Cristobal et al. 2006). Ladder or railroad channel designs have been used to synchronize the trajectories of two droplets (Ahn et al. 2011, Prakash & Gershenfeld 2007, L. Xu et al. 2012). These phenomena highlight the importance of considering the entire fluidic network in the bubble or droplet formation process, rather than merely the local fluid and interfacial dynamics. The availability of simple models helps to rationalize complex dynamical behaviors the larger the number of interconnected nozzles and channel segments.

6. CONCLUSIONS

Microfluidic generation of droplets and bubbles is entirely different from the generation of droplets and bubbles in unconfined geometries and is dominated by confinement of the interface. At low capillary numbers, fluid interfaces narrow and pinch off quasi-statically. Rectangular microchannels modulate breakup through flow in the corner gutters. Confinement effects remain at play even after viscous stresses become large enough to influence breakup. Confinement suppresses the growth of capillary instabilities, leading to the formation of persistent fluid threads. In less confined threads, absolute or convective instabilities can grow, resulting in variations in droplet size and uniformity. The confinement of fluid-fluid interfaces in microscale geometries, combined with low–Reynolds number and low-capillary number flows, is a primary reason for the superior control of droplet size and uniformity in microfluidic devices.

Confined droplets and bubbles also strongly influence the hydraulic resistance in a given channel. Changes in hydraulic resistance during the formation of droplets and bubbles lead to cross talk between multiple interconnected nozzles, limiting the ability to number up production of precise emulsions and foams. Creative microfluidic designs can mitigate these effects through the careful placement of low-resistance bypass channels that localize hydraulic resistance changes in a channel network and allow for the control of timing and motion of droplets and bubbles within devices. The ability to control the behavior of a multiphase fluidic network using simple hydraulic resistance concepts is one of the most powerful aspects of microfluidic design.

Surfactants and particles modulate interfacial properties in a variety of ways, but the main reason for their use in most microfluidics applications is to stabilize droplets and bubbles against coalescence. However, intermediate coverages of surfactants lead to interesting and useful behaviors that have yet to be fully exploited. Axial and lateral migration speeds of droplets are dramatically different at intermediate concentrations. Tip streaming of submicrometer-scale droplets occurs at moderate flow speeds and moderate concentrations, when timescales for surfactant adsorption, the rapid generation of a new interface, and the establishment of Marangoni stresses are all comparable. Particles can be loaded onto fluid interfaces at controlled rates and coverages, allowing for the design of interfacial mechanics and transport across interfaces.

Microfluidic applications of droplets and bubbles have benefited not just from the ability to generate extremely precise fluid volumes (i.e., without the formation of unwanted satellite droplets) at high frequencies, but also from a detailed understanding of the fluid dynamical phenomena that control breakup, motion, and coalescence when bubbles and droplets are confined within microscale geometries. Challenges remain in the ability to number up the production of multiphase materials while maintaining control of the volumes, volume fractions, and interfacial properties of individual fluid components. Part of the future success of these methods will rely on careful and creative engineering of the microfluidic network design to control hydraulic resistances and cross talk. Applications often rely on additional effects beyond fluid dynamics, such as transport of species to and along interfaces, and among the different bulk fluid phases. Understanding the mechanisms for transport of species at the microscale, and devising ways to control and isolate these mechanisms, will be essential to fully realizing the potential of multiphase microfluidics.

DISCLOSURE STATEMENT

The author is an inventor on a Harvard University patent related to droplet generation in flow-focusing microfluidic devices.

ACKNOWLEDGMENTS

The author gratefully acknowledges the graduate students who have worked with her in the area of microfluidic droplet formation and surfactant transport effects: Hans C. Mayer, Gordon F. Christopher, Nicolas J. Alvarez, Wingki Lee, Todd M. Moyle, Anthony P. Kotula, Sharon M. Vuong, Christopher W. Nelson, and Blake J. Bleier. The author has also benefited from a long-time collaboration with Lynn M. Walker, as well as helpful interactions with many other researchers in this area, including Michael R. Booty, Steven D. Hudson, Charles Maldarelli, Michael Siegel, Kathleen J. Stebe, and Howard A. Stone. The author's research in this area has been supported by the National Science Foundation, grants CBET-1033814, CBET-0730727, and CTS-0608864, as well as the American Chemical Society Petroleum Research Fund and the Pennsylvania Infrastructure Technology Alliance.

LITERATURE CITED

Abate AR, Mary P, van Steijn V, Weitz DA. 2012. Experimental validation of plugging during drop formation in a T-junction. *Lab Chip* 12:1516–21

Abkarian M, Subramaniam AB, Kim S-H, Larsen RJ, Yang S-M, Stone HA. 2007. Dissolution arrest and stability of particle-covered bubbles. *Phys. Rev. Lett.* 99:188301

Adzima BJ, Velankar SS. 2006. Pressure drops for droplet flows in microfluidic channels. *J. Micromech. Microeng.* 16:1504–10

Afkhami S, Leshansky AM, Renardy Y. 2011. Numerical investigation of elongated drops in a microfluidic T-junction. *Phys. Fluids* 23:022002

Ahn B, Lee K, Lee H, Panchapakesan R, Oh KW. 2011. Parallel synchronization of two trains of droplets using a railroad-like channel network. *Lab Chip* 11:3956–62

Al-Housseiny TT, Hernandez J, Stone HA. 2014. Preferential flow penetration in a network of identical channels. *Phys. Fluids* 26:042110

Alvarez NJ, Lee W, Walker LM, Anna SL. 2011. The effect of alkane tail length of C_iE_8 surfactants on transport to the silicone oil-water interface. *J. Colloid Interface Sci.* 355:231–36

Alvarez NJ, Walker LM, Anna SL. 2010. Diffusion-limited adsorption to a spherical geometry: the impact of curvature and competitive time scales. *Phys. Rev. E* 82:E011604

Anna SL, Bontoux N, Stone HA. 2003. Formation of dispersions using "flow focusing" in microchannels. *Appl. Phys. Lett.* 82:364–66

Anna SL, Mayer HC. 2006. Microscale tipstreaming in a microfluidic flow focusing device. *Phys. Fluids* 18:121512

Barbier V, Willaime H, Tabeling P, Jousse F. 2006. Producing droplets in parallel microfluidic systems. *Phys. Rev. E* 74:046306

Baret J-C, Kleinschmidt F, El Harrak A, Griffiths AD. 2009. Kinetic aspects of emulsion stabilization by surfactants: a microfluidic analysis. *Langmuir* 25:6088–93

Baroud CN, Tsikata S, Heil M. 2006. The propagation of low-viscosity fingers into fluid-filled branching networks. *J. Fluid Mech.* 546:285–94

Bazhlekov IB, Anderson PD, Meijer HEH. 2006. Numerical investigation of the effect of insoluble surfactants on drop deformation and breakup in simple shear flow. *J. Colloid Interface Sci.* 298:369–94

Belloul M, Engl W, Colin A, Panizza P, Ajdari A. 2009. Competition between local collisions and collective hydrodynamic feedback controls traffic flows in microfluidic networks. *Phys. Rev. Lett.* 102:194502

Binks BP. 2002. Particles as surfactants: similarities and differences. *Curr. Opin. Colloid Interface Sci.* 7:21–41

Blanchette F, Zhang WW. 2009. Force balance at the transition from selective withdrawal to viscous entrainment. *Phys. Rev. Lett.* 102:144501

Booty MR, Siegel M. 2010. A hybrid numerical method for interfacial fluid flow with soluble surfactant. *J. Comput. Phys.* 229:3864–83

Brugarolas T, Gianola DS, Zhang L, Campbell GM, Bassani JL, et al. 2014. Tailoring and understanding the mechanical properties of nanoparticle-shelled bubbles. *ACS Appl. Mater. Interfaces* 6:11558–72

Castro-Hernández E, Campo-Cortés F, Gordillo JM. 2012. Slender-body theory for the generation of micrometre-sized emulsions through tip streaming. *J. Fluid Mech.* 698:423–45

Chang C-H, Franses EI. 1995. Adsorption dynamics of surfactants at the air/water interface: a critical review of mathematical models, data, and mechanisms. *Colloids Surf. A* 100:1–45

Choi W, Hashimoto M, Ellerbee AK, Chen X, Bishop KJM, et al. 2011. Bubbles navigating through networks of microchannels. *Lab Chip* 11:3970–78

Christopher GF, Anna SL. 2007. Microfluidic methods for generating continuous droplet streams. *J. Phys. D* 40:R319–36

Christopher GF, Noharuddin NN, Taylor JA, Anna SL. 2008. Experimental observations of the squeezing-to-dripping transition in T-shaped microfluidic junctions. *Phys. Rev. E* 78:036317

Cristobal G, Benoit J-P, Joanicot M, Ajdari A. 2006. Microfluidic bypass for efficient passive regulation of droplet traffic at a junction. *Appl. Phys. Lett.* 89:034104

Cubaud T, Mason TG. 2008. Capillary threads and viscous droplets in square microchannels. *Phys. Fluids* 20:053302

de Bruijn RA. 1993. Tip-streaming of drops in simple shear flows. *Chem. Eng. Sci.* 48:277–84
de Lózar A, Juel A, Hazel AL. 2008. The steady propagation of an air finger into a rectangular tube. *J. Fluid Mech.* 614:173–95
De Menech M. 2006. Modeling of droplet breakup in a microfluidic T-shaped junction with a phase-field model. *Phys. Rev. E* 73:031505
De Menech M, Garstecki P, Jousse F, Stone HA. 2008. Transition from squeezing to dripping in a microfluidic T-shaped junction. *J. Fluid Mech.* 595:141–61
Dickinson E. 2013. Stabilising emulsion-based colloidal structures with mixed food ingredients. *J. Sci. Food Agric.* 93:710–21
Dollet B, van Hoeve W, Raven J-P, Marmottant P, Versluis M. 2008. Role of the channel geometry on the bubble pinch-off in flow-focusing devices. *Phys. Rev. Lett.* 100:034504
Eastoe J, Dalton JS. 2000. Dynamic surface tension and adsorption mechanisms of surfactants at the air–water interface. *Adv. Colloid Interface Sci.* 85:103–44
Eggers J. 1993. Universal pinching of 3D axisymmetric free-surface flow. *Phys. Rev. Lett.* 71:3458–60
Eggers J, Villermaux E. 2008. Physics of liquid jets. *Rep. Prog. Phys.* 71:036601
Eggleton CD, Stebe KJ. 1998. An adsorption-desorption-controlled surfactant on a deforming droplet. *J. Colloid Interface Sci.* 208:68–80
Ferri JK, Stebe KJ. 2000. Which surfactants reduce surface tension faster? A scaling argument for diffusion-controlled adsorption. *Adv. Colloid Interface Sci.* 85:61–97
Fuerstman MJ, Lai A, Thurlow ME, Shevkoplyas SS, Stone HA, Whitesides GM. 2007. The pressure drop along rectangular microchannels containing bubbles. *Lab Chip* 7:1479–89
Funfschilling D, Debas H, Li HZ, Mason TG. 2009. Flow-field dynamics during droplet formation by dripping in hydrodynamic-focusing microfluidics. *Phys. Rev. E* 80:015301
Gañán-Calvo AM. 2008. Unconditional jetting. *Phys. Rev. E* 78:026304
Gañán-Calvo AM, Gonzalez-Prieto R, Riesco-Chueca P, Herrada MA, Flores-Mosquera M. 2007. Focusing capillary jets close to the continuum limit. *Nat. Phys.* 3:737–42
Ganesan S, Tobiska L. 2012. Arbitrary Lagrangian–Eulerian finite-element method for computation of two-phase flows with soluble surfactants. *J. Comput. Phys.* 231:3685–702
Garstecki P, Fuerstman MJ, Stone HA, Whitesides GM. 2006. Formation of droplets and bubbles in a microfluidic T-junction: scaling and mechanism of break-up. *Lab Chip* 6:437–46
Garstecki P, Gitlin I, DiLuzio W, Whitesides GM, Kumacheva E, Stone HA. 2004. Formation of monodisperse bubbles in a microfluidic flow-focusing device. *Appl. Phys. Lett.* 85:2649–51
Garstecki P, Stone HA, Whitesides GM. 2005. Mechanism for flow-rate controlled breakup in confined geometries: a route to monodisperse emulsions. *Phys. Rev. Lett.* 94:164501
Glawdel T, Elbuken C, Ren C. 2011. Passive droplet trafficking at microfluidic junctions under geometric and flow asymmetries. *Lab Chip* 11:3774–84
Glawdel T, Elbuken C, Ren CL. 2012a. Droplet formation in microfluidic T-junction generators operating in the transitional regime. I. Experimental observations. *Phys. Rev. E* 85:016322
Glawdel T, Elbuken C, Ren CL. 2012b. Droplet formation in microfluidic T-junction generators operating in the transitional regime. II. Modeling. *Phys. Rev. E* 85:016323
Gopalan B, Katz J. 2010. Turbulent shearing of crude oil mixed with dispersants generates long microthreads and microdroplets. *Phys. Rev. Lett.* 104:054501
Gordillo JM, Sevilla A, Campo-Cortés F. 2014. Global stability of stretched jets: conditions for the generation of monodisperse micro-emulsions using coflows. *J. Fluid Mech.* 738:335–57
Guillot P, Colin A, Ajdari A. 2008. Stability of a jet in confined pressure-driven biphasic flows at low Reynolds number in various geometries. *Phys. Rev. E* 78:016307
Guillot P, Colin A, Utada AS, Ajdari A. 2007. Stability of a jet in confined pressure-driven biphasic flows at low Reynolds numbers. *Phys. Rev. Lett.* 99:104502
Gupta A, Kumar R. 2010. Flow regime transition at high capillary numbers in a microfluidic T-junction: viscosity contrast and geometry effect. *Phys. Fluids* 22:122001
Hashimoto M, Shevkoplyas SS, Zasonska B, Szymborski T, Garstecki P, Whitesides GM. 2008. Formation of bubbles and droplets in parallel, coupled flow-focusing geometries. *Small* 4:1795–805

Herrada MA, Gañán-Calvo AM, Guillot P. 2008. Spatiotemporal instability of a confined capillary jet. *Phys. Rev. E* 78:046312
Herrada MA, Gañán-Calvo AM, López-Herrera JM. 2011. Generation of small mono-disperse bubbles in axisymmetric T-junction: the role of swirl. *Phys. Fluids* 23:072004
Hoang DA, Portela LM, Kleijn CR, Kreutzer MT, van Steijn V. 2013. Dynamics of droplet breakup in a T-junction. *J. Fluid Mech.* 717:R4
Holt DJ, Payne RJ, Abell C. 2010. Synthesis of novel fluorous surfactants for microdroplet stabilisation in fluorous oil streams. *J. Fluor. Chem.* 131:398–407
Holtze C, Rowat AC, Agresti JJ, Hutchison JB, Angile FE, et al. 2008. Biocompatible surfactants for water-in-fluorocarbon emulsions. *Lab Chip* 8:1632–39
Hong J, Choi M, Edel JB, deMello AJ. 2010. Passive self-synchronized two-droplet generation. *Lab Chip* 10:2702–9
Humphry KJ, Ajdari A, Fernández-Nieves A, Stone HA, Weitz DA. 2009. Suppression of instabilities in multiphase flow by geometric confinement. *Phys. Rev. E* 79:056310
Husny J, Cooper-White JJ. 2006. The effect of elasticity on drop creation in T-shaped microchannels. *J. Non-Newton. Fluid Mech.* 137:121–36
Jakiela S, Makulska S, Korczyk PM, Garstecki P. 2011. Speed of flow of individual droplets in microfluidic channels as a function of the capillary number, volume of droplets and contrast of viscosities. *Lab Chip* 11:3603–8
Janssen PJA, Anderson PD. 2008. Surfactant-covered drops between parallel plates. *Chem. Eng. Res. Des.* 86:1388–96
Janssen PJA, Meijer HEH, Anderson PD. 2012. Stability and breakup of confined threads. *Phys. Fluids* 24:012102
Jensen MJ, Stone HA, Bruus H. 2006. A numerical study of two-phase Stokes flow in an axisymmetric flow-focusing device. *Phys. Fluids* 18:077103
Jeong W-C, Lim J-M, Choi J-H, Kim J-H, Lee Y-J, et al. 2012. Controlled generation of submicron emulsion droplets via highly stable tip-streaming mode in microfluidic devices. *Lab Chip* 12:1446–53
Jin F, Balasubramaniam R, Stebe KJ. 2004. Surfactant adsorption to spherical particles: the intrinsic length scale governing the shift from diffusion to kinetic-controlled mass transfer. *J. Adhes.* 80:773–96
Jin F, Gupta NR, Stebe KJ. 2006. The detachment of a viscous drop in a viscous solution in the presence of a soluble surfactant. *Phys. Fluids* 18:022103
Jin F, Stebe KJ. 2007. The effects of a diffusion controlled surfactant on a viscous drop injected into a viscous medium. *Phys. Fluids* 19:112103
Jullien MC, Ching MJTM, Cohen C, Menetrier L, Tabeling P. 2009. Droplet breakup in microfluidic T-junctions at small capillary numbers. *Phys. Fluids* 21:072001
Koester S, Angile FE, Duan H, Agresti JJ, Wintner A, et al. 2008. Drop-based microfluidic devices for encapsulation of single cells. *Lab Chip* 8:1110–15
Korczyk PM, Cybulski O, Makulska S, Garstecki P. 2011. Effects of unsteadiness of the rates of flow on the dynamics of formation of droplets in microfluidic systems. *Lab Chip* 11:173–75
Kotula AP, Anna SL. 2012. Probing timescales for colloidal particle adsorption using slug bubbles in rectangular microchannels. *Soft Matter* 8:10759–72
Krechetnikov R. 2012. Structure of Marangoni-driven singularities. *Phys. Fluids* 24:022111
Lee W, Walker LM, Anna SL. 2009. Role of geometry and fluid properties in droplet and thread formation processes in planar flow focusing. *Phys. Fluids* 21:032103
Leshansky AM, Pismen LM. 2009. Breakup of drops in a microfluidic T junction. *Phys. Fluids* 21:023303
Li W, Young EWK, Seo M, Nie Z, Garstecki P, et al. 2008. Simultaneous generation of droplets with different dimensions in parallel integrated microfluidic droplet generators. *Soft Matter* 4:258–62
Link DR, Anna SL, Weitz DA, Stone HA. 2004. Geometrically mediated breakup of drops in microfluidic devices. *Phys. Rev. Lett.* 92:054503
Liu H, Zhang Y. 2010. Phase-field modeling droplet dynamics with soluble surfactants. *J. Comput. Phys.* 229:9166–87
Marín AG, Campo-Cortés F, Gordillo JM. 2009. Generation of micron-sized drops and bubbles through viscous coflows. *Colloids Surf. A* 344:2–7

Martin JD, Hudson SD. 2009. Mass transfer and interfacial properties in two-phase microchannel flows. *New J. Phys.* 11:115005
Mazutis L, Baret J-C, Griffiths AD. 2009. A fast and efficient microfluidic system for highly selective one-to-one droplet fusion. *Lab Chip* 9:2665–72
Mazutis L, Griffiths AD. 2012. Selective droplet coalescence using microfluidic systems. *Lab Chip* 12:1800–6
McClements DJ. 2012. Advances in fabrication of emulsions with enhanced functionality using structural design principles. *Curr. Opin. Colloid Interface Sci.* 17:235–45
McDonald JCD, David C, Anderson JR, Chiu DT, Wu H, et al. 2000. Fabrication of microfluidic systems in poly(dimethylsiloxane). *Electrophoresis* 21:27–40
Moyle TM, Walker LM, Anna SL. 2012. Predicting conditions for microscale surfactant mediated tipstreaming. *Phys. Fluids* 24:082110
Moyle TM, Walker LM, Anna SL. 2013. Controlling thread formation during tipstreaming through an active feedback control loop. *Lab Chip* 13:4534–41
Mulligan MK, Rothstein JP. 2011. Deformation and breakup of micro- and nanoparticle stabilized droplets in microfluidic extensional flows. *Langmuir* 27:9760–68
Mulligan MK, Rothstein JP. 2012. Scale-up and control of droplet production in coupled microfluidic flow-focusing geometries. *Microfluid. Nanofluid.* 13:65–73
Musterd M, van Steijn V, Kleijn C, Kreutzer MT. 2015. Calculating the volume of elongated bubbles and droplets in microchannels from a top view image. *RSC Adv.* 5:16042–49
Nie Z, Seo M, Xu S, Lewis P, Mok M, et al. 2008. Emulsification in a microfluidic flow-focusing device: effect of the viscosities of the liquids. *Microfluid. Nanofluid.* 5:585–94
Olbricht WL. 1996. Pore-scale prototypes of multiphase flow in porous media. *Annu. Rev. Fluid Mech.* 28:187–213
Pan M, Rosenfeld L, Kim M, Xu M, Lin E, et al. 2014. Fluorinated Pickering emulsions impede interfacial transport and form rigid interface for the growth of anchorage-dependent cells. *ACS Appl. Mater. Interfaces* 6:21446–53
Papageorgiou DT. 1995. On the breakup of viscous liquid threads. *Phys. Fluids* 7:1529–44
Park JM, Hulsen MA, Anderson PD. 2013. Numerical investigation of the effect of insoluble surfactant on drop formation in microfluidic device. *Eur. Phys. J. Spec. Top.* 222:199–210
Parthiban P, Khan SA. 2012. Filtering microfluidic bubble trains at a symmetric junction. *Lab Chip* 12:582–88
Pawar AB, Caggioni M, Ergun R, Hartel RW, Spicer PT. 2011. Arrested coalescence in Pickering emulsions. *Soft Matter* 7:7710–16
Pompano RR, Liu W, Du W, Ismagilov RF. 2011. Microfluidics using spatially defined arrays of droplets in one, two, and three dimensions. *Annu. Rev. Anal. Chem.* 4:59–81
Prakash M, Gershenfeld N. 2007. Microfluidic bubble logic. *Science* 315:832–35
Priest C, Herminghaus S, Seemann R. 2006. Generation of monodisperse gel emulsions in a microfluidic device. *Appl. Phys. Lett.* 88:024106
Priest C, Reid MD, Whitby CP. 2011. Formation and stability of nanoparticle-stabilised oil-in-water emulsions in a microfluidic chip. *J. Colloid Interface Sci.* 363:301–6
Rayleigh L. 1879. On the capillary phenomena of jets. *Proc. R. Soc. Lond.* 29:71–97
Roché M, Aytouna M, Bonn D, Kellay H. 2009. Effect of surface tension variations on the pinch-off behavior of small fluid drops in the presence of surfactants. *Phys. Rev. Lett.* 103:264501
Romero PA, Abate AR. 2012. Flow focusing geometry generates droplets through a plug and squeeze mechanism. *Lab Chip* 12:5130–32
Rosenfeld L, Lin T, Derda R, Tang SKY. 2014. Review and analysis of performance metrics of droplet microfluidics systems. *Microfluid. Nanofluid.* 16:921–39
Sang L, Hong Y, Wang F. 2009. Investigation of viscosity effect on droplet formation in T-shaped microchannels by numerical and analytical methods. *Microfluid. Nanofluid.* 6:621–35
Schwalbe JT, Phelan FR Jr, Vlahovska PM, Hudson SD. 2011. Interfacial effects on droplet dynamics in Poiseuille flow. *Soft Matter* 7:7797–804
Shui L, van den Berg A, Eijkel JCT. 2011. Scalable attoliter monodisperse droplet formation using multiphase nano-microfluidics. *Microfluid. Nanofluid.* 11:87–92

Song H, Chen DL, Ismagilov RF. 2006. Reactions in droplets in microfluidic channels. *Angew. Chem. Int. Ed. Engl.* 45:7336–56
Steegmans MLJ, Schroën CGPH, Boom RM. 2009a. Generalised insights in droplet formation at T-junctions through statistical analysis. *Chem. Eng. Sci.* 64:3042–50
Steegmans MLJ, Schroën KGPH, Boom RM. 2009b. Characterization of emulsification at flat microchannel Y junctions. *Langmuir* 25:3396–401
Stoffel M, Wahl S, Lorenceau E, Höhler R, Mercier B, Angelescu DE. 2012. Bubble production mechanism in a microfluidic foam generator. *Phys. Rev. Lett.* 108:198302
Stone HA. 1994. Dynamics of drop deformation and breakup in viscous fluids. *Annu. Rev. Fluid Mech.* 26:65–102
Stone HA, Leal LG. 1990. The effects of surfactants on drop deformation and breakup. *J. Fluid Mech.* 220:161–86
Subramaniam AB, Mejean C, Abkarian M, Stone HA. 2006. Microstructure, morphology, and lifetime of armored bubbles exposed to surfactants. *Langmuir* 22:5986–90
Sugiura S, Nakajima M, Iwamoto S, Seki M. 2001. Interfacial tension driven monodispersed droplet formation from microfabricated channel array. *Langmuir* 17:5562–66
Sullivan MT, Stone HA. 2008. The role of feedback in microfluidic flow-focusing devices. *Philos. Trans. R. Soc. Lond. A* 366:2131–43
Suryo R, Basaran OA. 2006. Tip streaming from a liquid drop forming from a tube in a co-flowing outer fluid. *Phys. Fluids* 18:082102
Taylor GI. 1934. The formation of emulsions in definable fields of flow. *Proc. R. Soc. Lond. A* 146:501–23
Tetradis-Meris G, Rossetti D, Pulido de Torres C, Cao R, Lian G, Janes R. 2009. Novel parallel integration of microfluidic device network for emulsion formation. *Ind. Eng. Chem. Res.* 48:8881–89
Thorsen T, Roberts RW, Arnold FH, Quake SR. 2001. Dynamic pattern formation in a vesicle-generating microfluidic device. *Phys. Rev. Lett.* 86:4163–66
Tomotika S. 1935. On the instability of a cylindrical thread of a viscous liquid surrounded by another viscous fluid. *Proc. R. Soc. Lond. A* 150:322–37
Tseng Y, Prosperetti A. 2015. Local interfacial stability near a zero vorticity point. *J. Fluid Mech.* 776:5–36
Utada AS, Fernández-Nieves A, Gordillo JM, Weitz DA. 2008. Absolute instability of a liquid jet in a coflowing stream. *Phys. Rev. Lett.* 100:014502
Utada AS, Fernández-Nieves A, Stone HA, Weitz DA. 2007. Dripping to jetting transitions in coflowing liquid streams. *Phys. Rev. Lett.* 99:094502
van der Sman RGM, van der Graaf S. 2006. Diffuse interface model of surfactant adsorption onto flat and droplet interfaces. *Rheol. Acta* 46:3–11
van Dijke K, Veldhuis G, Schroen K, Boom R. 2009. Parallelized edge-based droplet generation (EDGE) devices. *Lab Chip* 9:2824–30
van Hoeve W, Gekle S, Snoeijer JH, Versluis M, Brenner MP, Lohse D. 2010. Breakup of diminutive Rayleigh jets. *Phys. Fluids* 22:122003
van Steijn V, Kleijn CR, Kreutzer MT. 2009. Flows around confined bubbles and their importance in triggering pinch-off. *Phys. Rev. Lett.* 103:214501
van Steijn V, Kleijn CR, Kreutzer MT. 2010. Predictive model for the size of bubbles and droplets created in microfluidic T-junctions. *Lab Chip* 10:2513–18
van Steijn V, Korczyk PM, Derzsi L, Abate AR, Weitz DA, Garstecki P. 2013. Block-and-break generation of microdroplets with fixed volume. *Biomicrofluidics* 7:024108
van Steijn V, Kreutzer MT, Kleijn CR. 2007. mu-PIV study of the formation of segmented flow in microfluidic T-junctions. *Chem. Eng. Sci.* 62:7505–14
Vladisavljević GT, Khalid N, Neves MA, Kuroiwa T, Nakajima M, et al. 2013. Industrial lab-on-a-chip: design, applications and scale-up for drug discovery and delivery. *Adv. Drug Deliv. Rev.* 65:1626–63
Wan J, Stone HA. 2012. Coated gas bubbles for the continuous synthesis of hollow inorganic particles. *Langmuir* 28:37–41
Wang K, Lu YC, Xu JH, Luo GS. 2009. Determination of dynamic interfacial tension and its effect on droplet formation in the T-shaped microdispersion process. *Langmuir* 25:2153–58

Wang Q, Siegel M, Booty MR. 2014. Numerical simulation of drop and bubble dynamics with soluble surfactant. *Phys. Fluids* 26:052102

Whitesides GM, Stroock AD. 2001. Flexible methods for microfluidics. *Phys. Today* 54:42–48

Wong H, Radke CJ, Morris S. 1995a. The motion of long bubbles in polygonal capillaries. Part 1. Thin films. *J. Fluid Mech.* 292:71–94

Wong H, Radke CJ, Morris S. 1995b. The motion of long bubbles in polygonal capillaries. Part 2. Drag, fluid pressure and fluid flow. *J. Fluid Mech.* 292:95–110

Xu JH, Dong PF, Zhao H, Tostado CP, Luo GS. 2012. The dynamic effects of surfactants on droplet formation in coaxial microfluidic devices. *Langmuir* 28:9250–58

Xu L, Lee H, Panchapakesan R, Oh KW. 2012. Fusion and sorting of two parallel trains of droplets using a railroad-like channel network and guiding tracks. *Lab Chip* 12:3936–42

Young YN, Booty MR, Siegel M, Li J. 2009. Influence of surfactant solubility on the deformation and breakup of a bubble or capillary jet in a viscous fluid. *Phys. Fluids* 21:072105

Annual Review of
Fluid Mechanics
Volume 48, 2016

Contents

Indexes

Errata

An online log of corrections to *Annual Review of Fluid Mechanics* articles may be found at http://www.annualreviews.org/errata/fluid